Water Science & Technology

IWA PUBLISHING

Water Science & Technology Vol 84 No 3, 499 doi: 10.2166/wst.2021.235

New g-C_3N_4/GO/MoS_2 composites as efficient photocatalyst for photocathodic protection of 304 stainless steel

Hongai Zheng [a], Xin Sun[a], Yue Liu[b], Shuangyan Jiang[a], Derui Wang[a], Yankun Fan[a], Lili Hu[a], Daquan Zhang[a], Weifeng Yao[a] and Lizhi Zhang[c,*]

[a] College of Environmental and Chemical Engineering, Shanghai University of Electric Power, Shanghai 200090, China
[b] Department of Production Safety, Shanghai Waterworks Fengxian Co., LTD, Shanghai 201499, China
[c] Department of Orthopedic Surgery, ShangHai YangPu District Central Hospital, YangPu Hospital Affiliated to TongJi University, No. 450 TengYue Road, Shanghai 200090, China
*Corresponding author. E-mail: drzhanglizhi001@163.com

HZ, 0000-0002-7162-852X

ABSTRACT

Photocathodic protection is an economical and environmental metal anticorrosion method. In this research, we successfully synthesized the g-C_3N_4/GO (15 wt%)/MoS_2 catalytic materials by a facile hydrothermal method. The results show that the as-prepared g-C_3N_4/GO (15 wt %)/MoS_2 composites prominently enhanced photocatalytic activities for the photocathodic protection of 304 stainless steel (SS) compared with the corresponding pristine g-C_3N_4 and MoS_2. Notably, the AC impedance results demonstrated that the *R*ct value of 304 SS coupled with g-C_3N_4/GO (15 wt%)/MoS_2 decreased to 35.66 Ω•cm^2, which is 29 and 37 times lower than that of g-C_3N_4 and MoS_2 alone. In addition, g-C_3N_4/GO (15 wt%)/MoS_2 provided the highest current density (77.19 μA•cm^2) for the 304 SS, which is four times that of pristine g-C_3N_4. All results indicate that as-prepared g-C_3N_4/GO (15 wt%)/MoS_2 photocatalysts have produced a distinct enhancement on photocathodic protection performance. An optimum decorating amount of MoS_2 onto g-C_3N_4 forms heterojunctions of g-C_3N_4/MoS_2, which favor the separation of electrons and holes efficiently. Furthermore, the addition of GO further promotes the separation and transfer of photo-induced carriers.

Key words: graphitic carbon nitride, heterojunction, photocathodic protection, photoelectrochemical

HIGHLIGHTS

- g-C_3N_4/GO/MoS_2 photocatalytic activity was enhanced to protect 304 stainless steel.
- The absorption boundary of g-C_3N_4/GO/MoS_2 was red-shifted toward the visible area.
- The photo-induced carriers' recombination of g-C_3N_4/GO/MoS_2 was inhibited.
- The 304 stainless steel was effectively protected when coupled to a photo-anode.

1. INTRODUCTION

With the rapid development of industry, energy shortage and environmental pollution have become the vital problems faced by human beings (Gao *et al.* 2018; He *et al.* 2018; Zhou *et al.* 2019). The utilization of solar energy has become a good solution to these serious problems. Therefore, the semiconductor photocatalyst has attracted increasing attention, and includes CO_2 photoreduction (Hashemizadeh *et al.* 2018; Xu *et al.* 2018), hydrogen generation (Mo *et al.* 2019), pollutant degradation (Xie *et al.* 2018), and photocathodic protection (PCP) (Guan *et al.* 2018b). Stainless steel materials can withstand high temperatures, oxidation resistance, and have superior mechanical properties, so they are widely used in industry, especially in environmental protection equipment, including delivery pipes, valves, water treatment equipment, and circulating cooling water systems (Ryan *et al.* 2002). However, stainless steel still has the risk of corrosion. Many factors induce corrosion in the water treatment system, including the microbial community in the sewage, low pH, and high salt concentration (Cui *et al.* 2016). Once the stainless steel device fails, it will cause huge economic losses. Therefore, it is very important to propose a reasonable anti-corrosion method (Liu *et al.* 2014; Chen *et al.* 2019). Compared to many metal anticorrosion methods, such as corrosion inhibitors (Fernandes *et al.* 2019; Sadeghi Erami *et al.* 2019), coating (Kiosidou *et al.* 2018; Rodriguez *et al.* 2018), and cathodic protection of sacrificial anodes (Zhang *et al.* 2012; Guan *et al.* 2018b), PCP is an economical and

environmental method with promising application prospects. Normally, a semiconductor is coated on the protected metal surface or acts as an anode through wires connected to the protected metal (Ren *et al.* 2016). Electrons of the semiconductor in the valence band (VB) excited by light, migrate into the conduction band (CB), and the corresponding holes generate in the VB (Jing *et al.* 2019). At the interface between semiconductor thin film and the solution, the holes (h^+) migrate to the surface of semiconductor particles and oxidize the electron donor (such as H_2O, OH^-), while electrons (e^-) migrate to the protected metal. As a result, the electron density on the surface of the protected metal increases and the corrosion potential shifts negatively so that the metal entered the thermodynamic and thermal stable region to achieve the purpose of cathodic protection. Therefore, in PCP, sufficiently negative CB potential is the postulate (Sun *et al.* 2015). TiO_2 coatings are the most widely used photocatalyst in PCP. But the band gap of TiO_2 is 3.2 eV, which limits its application in visible light range (Guan *et al.* 2018a). Many semiconductor materials have been developed used as photocatalysts in PCP including metal oxides (ZnO (Liu *et al.* 2019b), WO_3 (Ma *et al.* 2019), Fe_2O_3 (Liu *et al.* 2019a), *et al.*), metal sulfides (CdS (Vamvasakis *et al.* 2018), MoS_2 (Kong *et al.* 2018), *et al.*) and polymeric (g-C_3N_4 (Xu *et al.* 2019)). In recent years, g-C_3N_4, as a metal-free photocatalyst, has sparked extensive attention in photocatalysis due to its versatile properties, such as low cost, appropriate band gap (2.7 eV) for visible light absorption, good thermal stability, and optical properties (Wang *et al.* 2008; Ong *et al.* 2016; Wang *et al.* 2018b). However, the high recombination rate of photo-induced electrons and hole pairs is still a barrier for photocatalytic efficiency. A feasible way is constructing a heterojunction to overcome these disadvantages (Jiao *et al.* 2019). Heterojunction refers to the recombination of two semiconductors with matching band structures, one as an acceptor for electrons and the other as an acceptor for holes. When illuminated, the photoelectrons in the CB of one semiconductor will be transferred to the CB of another semiconductor to improve the efficiency of carrier transfer and separation (Li *et al.* 2020). Constructing g-C_3N_4 and other semiconductors (such as CdS, FeOCl, WO_3 and Ag_3PO_4) into a heterojunction framework can not only retain the advantages of each component separately, expand the photoresponse range, but also reduce the recombination of photogenerated electrons and holes, thereby improving photocatalytic performance (Katsumata *et al.* 2013; Du *et al.* 2021; Nguyen *et al.* 2021; You *et al.* 2021). It has been reported that the formation of rGO/Fe_2O_3/g-C_3N_4 nanocomposites exhibited superior photocatalytic ability by enhancing charge migration and separation (Shanavas *et al.* 2019).

Loading noble metals, such as Au and Pt, effectively improve the activity of photocatalysts. Recent studies have shown that MoS_2 can be applied as a substitution for noble metals in the integration of co-catalysts. Sun *et al.* (Liu *et al.* 2018) fabricated MoS_2 quantum dots on g-C_3N_4 and found that the composites markedly improved H_2 evolution activities. The enhancement of photocatalytic H_2 evolution was attributed to the formation of the heterojunction interface. The layered structure of MoS_2 is similar to graphene and can match with that of g-C_3N_4. Furthermore, researchers have confirmed the heterojunction formation between g-C_3N_4 and MoS_2 (Zhang *et al.* 2019b). Therefore, the g-C_3N_4/MoS_2 heterojunction promotes the migration and separation of photo-induced charge. GO has been introduced as an excellent electron conductive material that could promote the transport of photo-induced electrons and hole pairs in most ternary heterojunctions. Yet, as far as we know, there has been no previous report on g-C_3N_4/GO/MoS_2 as a ternary photocatalyst in PCP.

Based on the above issues, we constructed g-C_3N_4/GO/MoS_2 ternary semiconductor heterojunctions through a facile hydrothermal method, trying to develop a green and economical photocatalyst with good photocatalysis performance. The 304 SS was used to investigate the PCP performance of g-C_3N_4/GO/MoS_2. The ternary heterojunction composites exhibited high PCP performance. A possible mechanism of the catalyst promoting PCP was proposed.

2. EXPERIMENTS

2.1. Materials

The model of fluorine-doped tin oxide (FTO) conductive glass used in this experiment was FTO-P003, which was purchased from Zhuhai Kaivo Optoelectronic Technology Co., Ltd. The composition of 304 SS (wt%) is as follows: Fe (71.87), C (0.07), Cr (17.0), Ni (8.0), Mn (2.0), Si (1.0), P (0.035), and S (0.03). All the chemical reagents used in the experiments were analytically pure and were not further purified in the process of use.

2.2. Synthesis of layer g-C_3N_4

Here, 5 g of melamine was calcinated (heating rate: 2 °C/min) at 550 °C for 3 h in a tube furnace in nitrogen. Afterwards, the resulting bulk g-C_3N_4 was ground into powder in a mortar. Then, 0.5 g of g-C_3N_4 powder was calcinated (heating rate: 5 °C/

min) at 500 °C for 3 h in a tube furnace in air. Finally, the corresponding white layer of g-C_3N_4 product was collected (Papailias *et al.* 2018).

2.3. Synthesis of GO

Graphene oxide (denoted as GO) was prepared through oxidation of the natural graphite powder by a modified Hummers' method (Marinoiu *et al.* 2017, 2020). In detail, the mixture of 3.0 g graphite powder, 3.0 g P_2O_5, and 3.0 g $K_2S_2O_8$ was added into 50 mL of sulphuric acid (18.4 M). Next, the solution was heated to 80 °C and kept stirring for 5 h. The mixture was slowly diluted with 300 mL deionized (DI) water. Then the pre-oxidized graphite powder was obtained by filtration. In a next step, the pre-oxidized graphite power was put into 50 mL of sulphuric acid (18.4 M); 15 g $KMnO_4$ powder was slowly put under ice batches during stirring. After that, they were heated to 35 °C and kept for 2 h under stirring. After cooling down to room temperature, 20 mL of 30% H_2O_2 was added dropwise. Following that, the color of the mixture turned to golden yellow. Finally, the mixture was washed with diluted HCl solution (v:v = 1:10) by centrifugation. The as-obtained brown product was washed with DI water until the pH value was about 7.0.

2.4. Synthesis of g-C_3N_4/GO/MoS_2

The g-C_3N_4/GO/MoS_2 composites were achieved via a hydrothermal method. The amount of GO added was 15 wt%, and the mass ratio of g-C_3N_4 to MoS_2 was 1: 1. In a typical synthesis procedure, 0.1613 g of $Na_2MoO_4{\cdot}2H_2O$ and 0.2504 g of C_2H_5NS were dissolved into 60 mL DI water under magnetic stirring for 1 h. Subsequently, 2.13 g GO aqueous sol with 0.05 g g-C_3N_4 was dissolved into 20 mL DI water. The above two types of mixture solution were interfused completely. After that, the corresponding mixture solution was transferred into a 100 mL Teflon-lined autoclave and maintained at 180 °C for 24 h. Finally, the resulting dark precipitate denoting g-C_3N_4/GO (15 wt%)/MoS_2 was collected and fully washed with DI water and ethanol (Hu *et al.* 2018). Figure S1 in Supplementary Information is the illustration of the synthetic process for g-C_3N_4/GO (15 wt%)/MoS_2.

2.5. Characterization

The crystal structure of g-C_3N_4, MoS_2, and g-C_3N_4/GO (15 wt%)/MoS_2 was detected using a Bruker-D8 X-ray diffractometer (XRD, Bruker, Germany) with Cu$K\alpha$ radiation. X-ray photoelectron spectroscopy (XPS) was performed using a photoelectron spectrometer (Kalpha, ThermoFisher, USA). Characterization of the morphology of g-C_3N_4, MoS_2, and g-C_3N_4/GO (15 wt %)/MoS_2 was performed using a supra 55 field emission scanning electron microscope (FE-SEM, Zeiss, Germany). Transmission electronic microscopy (TEM) images and element mapping of materials were analyzed using a JMT-2100F electron microscope (JEOL, Japan), equipped with a Super-X, energy-dispersive spectrometer (EDS, Bruker Germany). A UV-2550 spectrophotometer (SHIMADZU, Japan) was used to conduct ultraviolet-visible diffuse reflectance absorption spectra (UV-vis) of the samples. The photoluminescence properties of samples were determined using a RF-5301PC spectrofluorophotometer (Shimadzu, Japan) with an excitation wavelength of 400 nm.

2.6. Photoelectrochemical experiment

The electrochemical experiment was carried out with a set of self-made electrochemical testing equipments, the schematic diagram of which is shown in Figure S2.

Two beakers acted as photochemical cell and electrochemical cell. The electrolyte in the photochemical cell was 0.1 M Na_2S and 0.2 M NaOH, and the electrolyte in the electrochemical cell was 3.5 wt% NaCl. The two beakers were connected by a salt bridge.

In the electrochemical cell, the Pt sheet was used as the counter electrode, the calomel electrode was used as the reference electrode, and the 304 SS electrode coupled with the photoelectrode acted as the working electrode. The light source was a 300 W xenon lamp (PLS-SXE300) with a light intensity of 520 MW/cm^2, which shone directly on the back of the light electrode. The distance between the light source and the light electrode was 5 cm (Zhang *et al.* 2014).

Preparation of the salt bridge: 3 g agar powder was dissolved in 100 mL DI water and heated to 90 °C until completely dissolved, followed by the addition of 34.2 g potassium chloride. Subsequently, the above solution was transferred to a U-shaped tube with a rubber dropper and cooled to room temperature.

Preparation of the 304 SS electrode: the 304 SS was cut into small pieces of 10 mm × 10 mm × 3 mm and polished step by step with sandpaper. A copper wire was welded to the back of the 304 SS sheet, followed by sealing with epoxy resin, and then polished evenly with 2,000 mesh SiC papers, so that the exposed surface (working surface) area of the 304 SS sheet

was 10 mm × 10 mm. Finally, the above electrode was washed in ethanol with ultrasound for 30 min, then rinsed with DI water, and dried in a drying oven (room temperature) for 24 h for later use.

Preparation of the photoelectrode: the FTO was cut into small pieces of 10 mm × 20 mm and put into the cleaning solution (10 mL DI water + 10 mL isopropyl alcohol + 10 mL acetone) with ultrasonic vibration for 30 min, then rinsed with DI water, followed by sealing the resulting FTO surface with tape, leaving only a 10 mm × 10 mm area as a working surface. Afterwards, 20 mg of photocatalyst, 20 μL naphthol, and 1 mL of ethanol were mixed in a centrifuge tube. After ultrasonic (100 W/40 kHz) bombardment for 30 min, the corresponding slurry was collected. Finally, 20 μL of the slurry was smeared onto the working surface of the FTO as evenly as possible to ensure the same sample mass on the FTO surface (about 0.4 mg/cm^2). After natural air drying, the obtained photoelectrode was heated to 100 °C for 2 h.

CHI660D electrochemical workstation was used to measure the electrochemistry performance of 304 SS coupled with different photocatalysts. Electrochemical impedance spectroscopy (EIS) tests were carried out in the frequency between 10^5 and 10^{-2} Hz, and the AC voltage amplitude was 5 mV. Dynamic potential polarization curves (Tafel plot) were tested with a scan rate of 1 mV·s^{-1}. The linear sweep voltammetry (*i-V*) measurement was obtained from −1.0 V to 0.4 V (vs. SCE) with a scan rate of 0.02 mV·s^{-1}. The time gap between light and dark was 10 s. The CV curves test was performed with a scan rate of 10 mV. The Mott–Schottky curves were tested from −1.0 to 0.0 V (vs. SCE). The AC voltage amplitude was 10 mV, and the test frequency was 1,000 Hz.

3. RESULTS AND DISCUSSION

3.1. Structure and morphology analysis

The crystal structure of g-C_3N_4, MoS_2, and g-C_3N_4/GO (15 wt%)/MoS_2 was analyzed by XRD. From Figure 1, we can see that at 13.0° and 27.4°, the characteristic diffraction peaks of g-C_3N_4 exhibited corresponding to (100) and (002) planes (JCPDS 87-1526) (Yang *et al.* 2020). The weak peak at 13.0° was derived from the in-plane structural repeated motif of tri-s-triazine units with an interplanar distance of $d = 0.663$ nm (Wang *et al.* 2018c). The dominant peak, which was at 27.4°, was derived from the aromatic ring system stack whose interplanar distance was 0.324 nm (Wang *et al.* 2018a). As for MoS_2 samples, the two diffraction peaks at 33.3° and 58.8° corresponded well to MoS_2 (JCPDS 37-1492) (Zhang *et al.* 2019a), which represented the (101) and (110) crystal planes, respectively. The 13.9° diffraction peak corresponding to the (002) crystal plane appeared at 10.3°, which was due to its interlayer expansion effect (Zhang *et al.* 2020). According to the Bragg equation: $2d\sin\theta = \lambda$, the interlayer spacing of the (002) plane of the MoS_2 sample could be calculated. The interplanar distance was about 0.86 nm. In g-C_3N_4/GO (15 wt%)/MoS_2 composites, the main performance was the characteristic peak of MoS_2, and the peak height was decreased. This was because the sample contains g-C_3N_4 and GO, which resulted in a decrease in its crystallinity. The reason for the weak characteristic peak of g-C_3N_4 was that the high crystalline MoS_2 grew on the surface of g-C_3N_4 (Fageria *et al.*

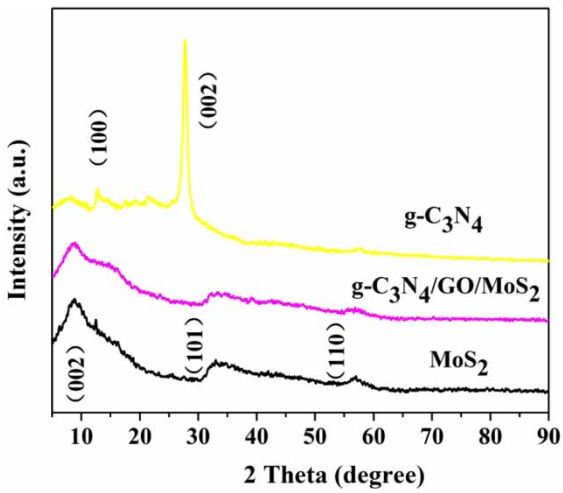

Figure 1 | XRD patterns of g-C_3N_4, MoS_2, and g-C_3N_4/GO (15 wt%)/MoS_2.

2017). In addition, no characteristic peak of GO was observed in g-C_3N_4/GO (15 wt%)/MoS_2 samples, which was due to the relatively low GO content (Guan *et al.* 2017).

XPS spectra recorded the surface electronic states and chemical composition of ternary composites. Figure S3a indicated the spectrum of g-C_3N_4/GO (15 wt%)/MoS_2 demonstrated the co-existence of Mo, S, C, O, and N elements. As shown in Figure S3b, the peak at 284.16 eV showed the occurrence of sp^2 C = C bonds of g-C_3N_4 (Shao *et al.* 2016). The peak at 285.64 eV can be consistent with sp^3 hybridized C atoms (C-$(N)_3$) (Fu *et al.* 2018). The peak located at 288.20 eV was ascribed to the sp^2 carbon N-C = N, which was in the N-containing aromatic rings (Fu *et al.* 2018). Figure S3c shows N 1s spectrum, the peak at 398.49 eV was attributed to C-*N* = C groups. The peak at 400.23 eV showed the occurrence of the tertiary nitrogen N-$(C)_3$ groups (Sun *et al.* 2020). In addition, the peak at 404.46 eV may be associated with positive charge localization or the charging effects in the heterocycles (Wang *et al.* 2020). As can be seen in Figure S3d, the peak centered located at 531.53 eV correspond to O 1s orbital (Hu *et al.* 2018). In Figure S3e, the S 2p peaks, which were located at 161.53 eV and 162.95 eV, were consistent with S $2p_{3/2}$ and S $2p_{1/2}$ of S^{2-}, respectively (Guan *et al.* 2017). In addition, the peak located at 164.23 eV corresponds to the C–S bond formed by replacing sulfur with lattice nitrogen in the g-C_3N_4 framework (Bai *et al.* 2018). Figure S3f shows the Mo 3d high-resolution XPS spectrum of the g-C_3N_4/GO (15 wt%)/MoS_2 sample. The peaks located at 232.41 eV and 228.89 eV corresponded to Mo $3d_{3/2}$ and Mo $3d_{5/2}$ of Mo^{4+} in MoS_2, respectively (Zhou *et al.* 2020). The peak at 235.65 eV was consistent with the Mo atoms exposed on the surface (Ou *et al.* 2020). The weak peak at 226.03 eV can be ascribed to S^{2-} and Mo^{4+}, which is the typical peak for MoS_2 (Bai *et al.* 2018).

The morphology of the ternary composites was further characterized by SEM. The g-C_3N_4 exhibited an average of 100 nm thicknesses with a lamellar stackable structure. In the MoS_2/GO composites, MoS_2 was in the form of nanoparticles, and the wrinkle GO was enclosed on the surface of MoS_2 (Figure S4a and 4b). As for the sample, the wrinkles GO wrapped MoS_2 nanoparticles attached to the surface of the g-C_3N_4 sheet layer (Figure S4c). Figure S4d indicated the co-existence of C, N, O, S, and Mo elements in the g-C_3N_4/GO (15 wt%)/MoS_2 sample.

The morphologies of g-C_3N_4/GO (15 wt%)/MoS_2 samples were further observed by TEM. MoS_2 was a petal-shaped nanosheet. MoS_2 nanosheets grew on g-C_3N_4 (Figure S5a). Figure S5b shows the HR-TEM images of g-C_3N_4/GO (15 wt %)/MoS_2. Each petal of MoS_2 nanosheets displayed obvious lattice fringes with a lattice spacing of 0.86 nm, corresponding to the (002) crystal plane of MoS_2. MoS_2 and g-C_3N_4 were closely attached, and the crystal lattices of both could be clearly seen. Figure S5c further demonstrates the co-existence of C, N, O, S, and Mo elements in the g-C_3N_4/GO (15 wt%)/MoS_2 sample.

3.2. Optical properties

The UV-vis DRS of g-C_3N_4, MoS_2,g-C_3N_4/MoS_2, g-C_3N_4/GO (15 wt%)/MoS_2 are depicted in Figure S6. The visible light absorption threshold of g-C_3N_4 was 410 nm. MoS_2 samples were black and therefore absorbed in the visible range (Zhang *et al.* 2019b). After adding MoS_2, the g-C_3N_4/MoS_2 composites showed strong light absorption ability, and the heterostructure formed between them. g-C_3N_4/GO (15 wt%)/MoS_2 had stronger absorption in the visible light region than g-C_3N_4/MoS_2 composites. This was due to the addition of GO, which absorbed light in the full spectral range, thereby increasing the visible light absorption of the composite. Using the Kubelka–Munk equation, the Eg of the obtained sample was calculated:

$$ahv = A(hv - Eg)^{n} \tag{1}$$

where α, h, v, A, and Eg represent absorption coefficient, Planck constant, light frequency, constant and band-gap energy, respectively. The value of n depends on the transition characteristic of the material, $n = 1/2$ for direct transition and $n = 2$ for indirect transition. g-C_3N_4 and MoS_2 were indirect transitions photocatalysts. The band gap of g-C_3N_4 was calculated to be 2.81 eV. For MoS_2, g-C_3N_4/$MoS_2$and g-C_3N_4/GO (15 wt%)/MoS_2 samples, the band gaps were calculated as 1.51 eV, 1.71 eV, and 1.87 eV, respectively.

At an excitation wavelength of 400 nm, the PL spectra of MoS_2, g-C_3N_4/MoS_2 and g-C_3N_4/GO (15 wt%)/MoS_2 composites are displayed in Figure S7. Two emission peaks were observed, which appeared at 450 and 470 nm (Liang *et al.* 2020). The emission peak of MoS_2 was the strongest, and indicated that the high recombination efficiency of photo-generated carriers. After adding g-C_3N_4, the peak value decreased, indicating that the separation of photo-generated carriers had been promoted. The emission peak of g-C_3N_4/GO (15 wt%)/MoS_2 composites was the weakest, indicating that the addition of GO promoted

the transfer of photogenerated electrons and holes. Therefore, the g-C_3N_4/GO (15 wt%)/MoS_2 ternary composites showed the strongest photoelectrochemical activity.

3.3. Photocathodic protection performance

To investigate the photoelectrochemical performance of the composite catalyst, photogenerated current density (*I-T*) was performed at interval of 50 s/time illumination. As shown in Figure 2, after illumination, the photocurrent density of the samples increased. The greater the increase in photogenerated current density, the higher was the charge separation efficiency of the catalyst. The photocurrent of MoS_2 alone was relatively low, and the photocurrent significantly increased after being combined with g-C_3N_4, which reached 6 μA/cm^2. g-C_3N_4/GO (15 wt%)/MoS_2 has the best photocurrent response, which can reach 22 μA/cm^2. This is because the heterostructure of g-C_3N_4/MoS_2 increased the electron-hole separation efficiency, and the addition of GO was more conducive to the photogenerated electron transfer between g-C_3N_4/MoS_2.

EIS test is an effective method to analyze and evaluate the PCP performance of samples. Figure 3 shows the EIS Nyquist plots and equivalent circuit diagram of 304 SS coupled with different photoelectrodes in light. The 304 SS coupled with g-

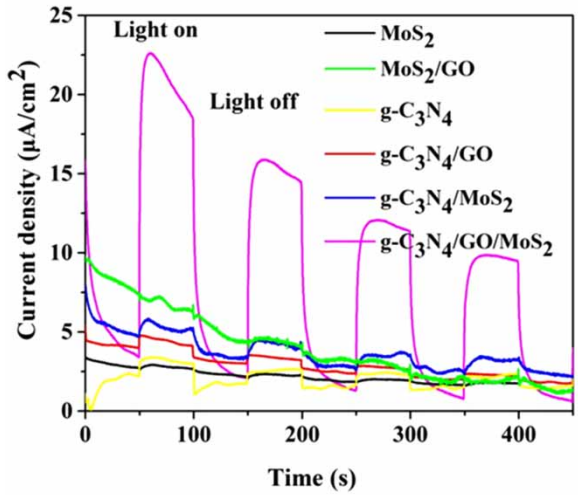

Figure 2 | Photogenerated current density of g-C_3N_4, MoS_2, and g-C_3N_4/GO (15 wt%)/MoS_2 composites photocatalytic under intermittent visible light.

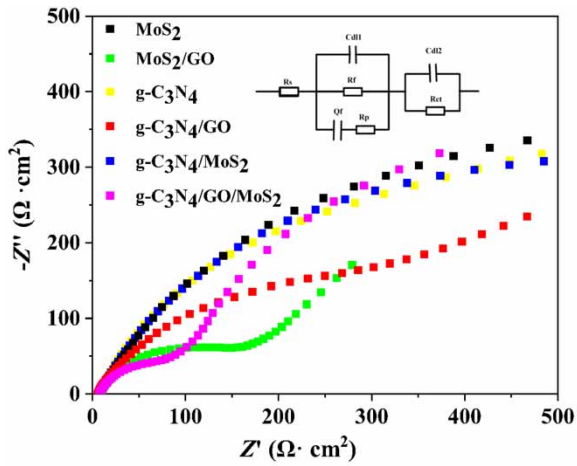

Figure 3 | (a) Nyquist plots of 304 SS coupled with the photoelectrodes under illumination conditions. The inset is the equivalent circuit by EIS results fitting.

C_3N_4/MoS_2 showed an obvious and smaller capacitive reactance arc than pure g-C_3N_4 and MoS_2. After adding GO, two arcs appeared in the low-frequency region. The small semi-circular arc indicated low charge transfer resistance (Wei *et al.* 2019). As shown in Figure 3, the equivalent circuit as R (CR(QR)) (CR) fitting circuit was adopted to fit the EIS results using the ZSimpWin software, where *C*dl and *Q*f represent the double-layer capacitance and the capacitance of the surface film, respectively. Furthermore, *R*s, *R*f, *R*p, and *R*ct represent the electrolyte solution resistance, the resistance of oxide films, electrolyte, and charge transfer, respectively. Y and n are constants that are independent of frequency. Detailed fitting data of the impedance spectrum of the material are shown in Table 1. *R*ct values can be used to characterize the charge transfer resistance of semiconductor materials. The *R*ct coupled with g-C_3N_4 and MoS_2 was 1,032 Ω•cm^2 and 1,324 Ω•cm^2, respectively. The *R*ct coupled with g-C_3N_4/MoS_2 was 967.9 Ω•cm^2, indicating that the heterostructure reduced the charge transfer resistance of the composites. After adding GO, the *R*ct values decreased significantly. The decrease in *R*ct value indicated the higher photogenerated electrons transfer. The EIS results showed that the g-C_3N_4/GO (15 wt%)/MoS_2 composites transferred a large number of electrons to the surface of 304 SS, resulting in the best photochemical cathodic protection performance.

Figure 4 demonstrates the Tafel plot of 304 SS coupled with kinds of photoelectrodes in light. The corresponding parameters calculated are displayed in Table 2. The potential of 304 SS coupled with g-C_3N_4/MoS_2 was between that of g-C_3N_4 and MoS_2. After adding GO, the corrosion potentials of 304 SS coupled with all three samples significantly shifted negatively. 304 SS coupled with g-C_3N_4/GO showed the most negative corrosion potential. As for the corrosion current, g-C_3N_4/MoS_2 was higher than that of MoS_2 and g-C_3N_4 alone, which is ascribed to the formation of heterojunctions. The increase in the corrosion current increased the electron transfer rate (Qiu *et al.* 2020). After the introduction of GO, the corrosion

Table 1 | Fitting impedance parameters of Nyquist plots of composites

Samples	*R*s (Ω·cm^2)	*C*dl1 (F)	*R*f (Ω·cm^2)	*Q*f		*R*p (Ω·cm^2)	*C*dl2 (F)	*R*ct (Ω·cm^2)
				y (μS·s^n·cm^{-2})	n			
g-C_3N_4	5.495	8.452×10^{-7}	691.5	7.318×10^{-4}	0.7553	1.411	9.654×10^{-3}	1,032
MoS_2	3.932	2.875×10^{-7}	848.6	5.906×10^{-4}	0.7395	3.916	9.105×10^{-3}	1,324
g-C_3N_4/GO	6.013	2.712×10^{-7}	495.6	6.188×10^{-4}	0.634	0.7813	8.825×10^{-3}	552.8
MOS_2/GO	3.807	1.571×10^{-7}	190.2	5.523×10^{-4}	0.7445	4.272	1.342×10^{-2}	359.4
g-C_3N_4/MoS_2	4.362	3.569×10^{-7}	750.6	5.907×10^{-4}	0.7533	2.93	9.564×10^{-3}	967.9
g-C_3N_4/GO (15 wt%)/MoS_2	2.604	8.916×10^{-8}	3,690	2.997×10^{-3}	0.5715	4.463	2.408×10^{-4}	35.66

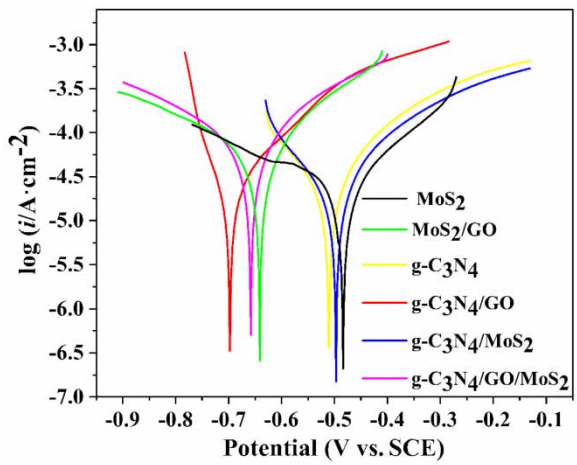

Figure 4 | Tafel plots of 304 SS coupled with photoanodes under illumination.

Table 2 | Electrochemical parameters obtained by the Tafel curves of 304 SS coupled with photoanodes under illumination

Samples	E_{corr} (V vs.SCE)	βc (mv dec^{-1})	βa (mv dec^{-1})	j_{corr} (μA cm^{-2})
MoS_2	−0.484	32.65	54.70	10.74
MoS_2/GO	−0.641	36.87	60.82	62.97
g-C_3N_4	−0.511	75.46	92.35	17.49
g-C_3N_4/GO	−0.698	31.69	57.62	35.59
g-C_3N_4/MoS_2	−0.497	76.61	94.83	18.95
g-C_3N_4/GO (15 wt%)/MoS_2	−0.658	40.47	56.08	77.19

currents of 304 SS coupled with g-C_3N_4 and MoS_2 significantly increased. GO promoted the transfer of photo-generated electrons and holes. 304 SS coupled with g-C_3N_4/GO (15 wt%)/MoS_2 revealed the highest current density, which was 77.19 μA•cm^{-2}. The heterojunction of g-C_3N_4/MoS_2 promoted the separation of photogenerated electrons and holes, and the addition of GO promoted the transfer of photo-generated electrons and holes.

3.4. Photoelectrochemical measurements

To study the photoelectrochemical performance of the composite photocatalyst further, the photoinduced *i-V* curves of the composites between −1.0 and 0.4 V were measured under intermittent light. The photoelectrochemical properties of the composites were tested by intermittent illumination of 10 s (Figure 5). The samples generated the zigzag photocurrent response between −1.0 and 0.4 V. Comparing the absolute value of photocurrent of different samples, the photo-generated current density produced by g-C_3N_4/GO (15 wt%)/MoS_2 was the highest. The g-C_3N_4/GO (15 wt%)/MoS_2 showed the best photoelectrochemical properties.

The CV curves of the 304 SS coupled with samples were also tested under light. The results are shown in Figure 6. In this experiment, the CV curves of 304 SS coupled with different photocatalysts were tested at a scan rate of 10 mv. The potential ranges of the samples were approximately −0.2 V to 0.4 V. 304 SS coupled with MoS_2 showed double capacitance characteristics. The cathode and anode peaks of other photocatalysts were not the same (Fageria *et al.* 2017). According to the Randles–Sevcik equation, the electroactive surface area (ECSA) was proportional to the peak of the cathode and anode (Shi & Zhao 2014). The larger ECSA means more active sites for the electrochemical reaction. The high cathode and anode peak value generated a larger ECSA. In addition, it exhibited better electrochemical performance. In Figure 6, we can see that the 304 SS coupled with g-C_3N_4/GO (15 wt%)/MoS_2 showed the highest peak in the cathode and anode curves. Therefore, the ternary photocatalyst has once again been proved to have the best electrochemical performance.

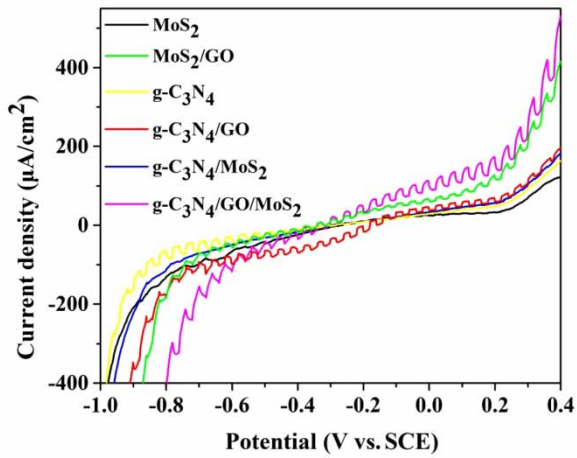

Figure 5 | Photoinduced I–V curves of g-C_3N_4, MoS_2, and g-C_3N_4/GO (15 wt%)/MoS_2 composites under intermittent visible light.

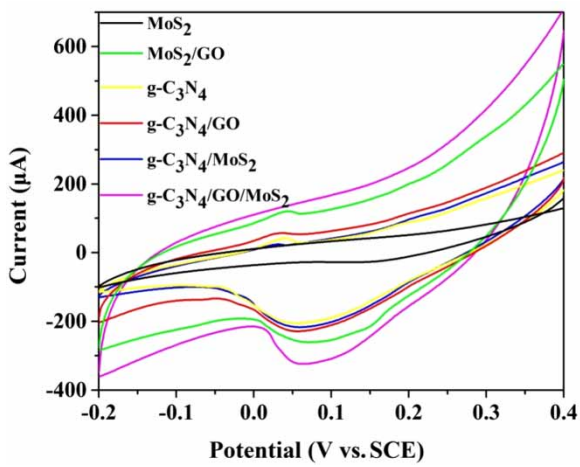

Figure 6 | CV curves of 304 SS coupled with g-C_3N_4, MoS_2, and g-C_3N_4/GO (15 wt%)/MoS_2 composites under illumination.

3.5. Mechanism

To explore the mechanism of PCP on composites photocatalyst, Mott–Schottky plots were performed. According to the formula listed, we calculated the flat band potential as follows:

$$\frac{1}{C^2} = 2(e\varepsilon\varepsilon_0 N_D)^{-1} \cdot \left(E - E_{FB} - \frac{kT}{e}\right) \tag{2}$$

C represented the capacitance of the space charge region. e was the electronic charge. ε was the relative dielectric constant of the semiconductor. ε_0 represented the permittivity for free space. N_D was the charge carrier density. E was the applied potential. E_{FB} was the flat band potential. T was the temperature. k was the Boltzmann constant (Jing *et al.* 2019). The flat band potential (E_{FB}) was determined from the horizontal intercept. As shown in Figure 7, the E_{FB} of MoS_2 was about -0.93 eV. After adding GO, its E_{FB} was negatively shifted to -0.99 eV. The E_{FB} of g-C_3N_4 was about -0.83 eV. After

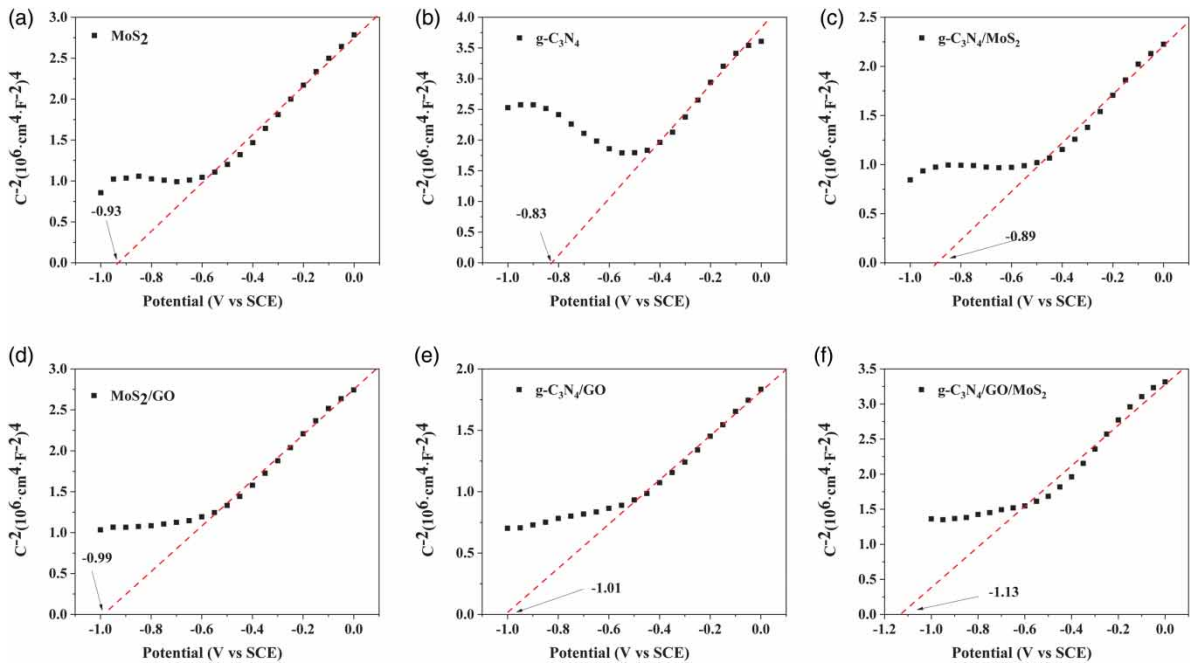

Figure 7 | Mott–Schottky plots of g-C_3N_4, MoS_2, and g-C_3N_4/GO (15 wt%)/MoS_2 composites under illumination.

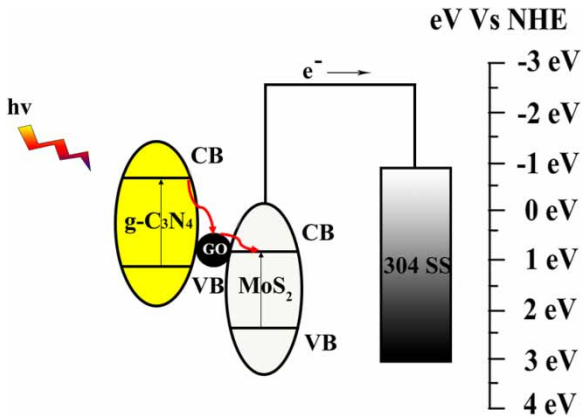

Figure 8 | The photocathodic protection mechanism of g-C_3N_4/GO (15 wt%)/MoS_2 composites.

adding GO, its E_{FB} was negatively shifted to −1.01 eV. The negative shift of E_{FB} increases the Fermi level of the material, which was more favorable for the transfer of photogenerated electrons (Liu *et al.* 2018; Ou *et al.* 2020). Through GO modification, the E_{FB} of a photocatalyst was negatively shifted, which improved the transfer efficiency of photogenerated electrons and holes, thereby improving the photocathodic protection ability of the composites. The E_{FB} of g-C_3N_4/MoS_2 was −0.89 eV, which was between the MoS_2 and g-C_3N_4. After GO was compounded with g-C_3N_4/MoS_2, the E_{FB} was negatively shifted to −1.13 eV. This indicated that g-C_3N_4/GO (15 wt%)/MoS_2 had better photogenerated charge separation efficiency and more excellent photocathodic protection performance.

Based on the results of the aforementioned experiments, the possible mechanism of the catalyst promoting PCP is proposed in Figure 8. Under visible light, the CB of g-C_3N_4 and MoS_2 both generated photogenerated electrons and left the photogenerated holes on the VB. In the g-C_3N_4/GO (15 wt%)/MoS_2 sample, g-C_3N_4 and MoS_2 formed the heterojunction. Photogenerated electrons transferred from the CB of g-C_3N_4 to the CB of MoS_2. The formation of the heterojunction electric field promoted the separation of photogenerated electrons and holes. The addition of GO further promoted the separation and transfer of photogenerated electrons and holes and simultaneously reduced the Fermi level of the composites. The photoelectrons on the surface of the samples transferred to the 304 SS surface through the wire, which made the self-corrosion potential of 304 SS drop sharply and resulted in the cathodic polarization of 304 SS.

4. CONCLUSION

In this research, the g-C_3N_4/GO (15 wt%)/MoS_2 composites were successfully synthesized by a facile hydrothermal method. MoS_2 was a petal-shaped nanosheet characterized by SEM and TEM. Wrinkled GO wrapped MoS_2 nanoparticles attached to the surface of the g-C_3N_4 sheet. The EIS results depicted that the *R*ct value of 304 SS coupled with g-C_3N_4/MoS_2 decreased from 1,032 to 967.9 Ω•cm^2 compared with g-C_3N_4 alone. Notably, the *R*ct value of 304 SS coupled with g-C_3N_4/GO (15 wt %)/MoS_2 composites decreased to 35.66 Ω•cm^2, which was 29 and 37 times lower than that of g-C_3N_4 and MoS_2 alone.

The polarization curve fitting values exhibited that g-C_3N_4/GO (15 wt%)/MoS_2 provided the highest current density (77.19 μA•cm^2) for the 304 SS, which was four times higher than that of single g-C_3N_4. The mechanism is that, under light conditions, photo-generated electrons were generated from the CB of g-C_3N_4 and transferred to the VB of MoS_2, and the heterojunction formed between g-C_3N_4 and MoS_2. The formation of a heterojunction electric field promoted the separation of photogenerated electrons and holes. The addition of GO further promoted the separation and transfer of photogenerated electrons and holes and simultaneously reduced the Fermi level of the composites. Therefore, the ternary composite improved the photocathode protection performance for 304 SS. This research is expected to provide new insights to explore high-efficiency photocatalysts and new corrosion protection technologies with potential application prospects.

ACKNOWLEDGEMENTS

Research was supported by the Grant from National Natural Science Foundation of China (81572218, 21776172, 52071198), Science and Technology Commission of Shanghai Municipality (Shanghai Municipal Natural Science Foundation,

13ZR1439100) and Shanghai Municipal Bureau of Health (20124303). The research was supported by the Shanghai Engineering Research Center of Energy-Saving in Heat Exchange Systems.

DECLARATION OF INTERESTS

The authors declare that they have no known competing financial interests or personal relationships that could have appeared to influence the work reported in this paper.

DATA AVAILABILITY STATEMENT

All relevant data are included in the paper or its Supplementary Information.

REFERENCES

Bai, J. R., Lv, W. H., Ni, Z. J., Wang, Z. L., Chen, G., Xu, H. Y., Qin, H. F., Zheng, Z. & Li, X. 2018 Integrating MoS_2 on sulfur-doped porous g-C_3N_4 isotype heterojunction hybrids enhances visible-light photocatalytic performance. *Journal of Alloys and Compounds* **768**, 766–774.

Chen, C., Wang, Y., Liu, S., Feng, R., Gu, X. & Qiao, C. 2019 Research on the application of compound microorganism preparation in reusing urban reclaimed water in circulating cooling water system. *Water Science and Technology* **80** (9), 1763–1773.

Cui, Y., Liu, S., Smith, K., Yu, K., Hu, H., Jiang, W. & Li, Y. 2016 Characterization of corrosion scale formed on stainless steel delivery pipe for reclaimed water treatment. *Water Research* **88**, 816–825.

Du, J., Xu, Z., Li, H., Yang, H., Xu, S., Wang, J., Jia, Y., Ma, S. & Zhan, S. 2021 Ag_3PO_4/g-C_3N_4 Z-scheme composites with enhanced visible-light-driven disinfection and organic pollutants degradation: uncovering the mechanism. *Applied Surface Science* **541**, 148487.

Fageria, P., Sudharshan, K. Y., Nazir, R., Basu, M. & Pande, S. 2017 Decoration of MoS_2 on g-C_3N_4 surface for efficient hydrogen evolution reaction. *Electrochimica Acta* **258**, 1273–1283.

Fernandes, C. M., Alvarez, L. X., dos Santos, N. E., Maldonado Barrios, A. C. & Ponzio, E. A. 2019 Green synthesis of 1-benzyl-4-phenyl-1H-1,2,3-triazole, its application as corrosion inhibitor for mild steel in acidic medium and new approach of classical electrochemical analyses. *Corrosion Science* **149**, 185–194.

Fu, Y. H., Liang, W., Guo, J. Q., Tang, H. & Liu, S. S. 2018 MoS_2 quantum dots decorated g-C_3N_4/Ag heterostructures for enhanced visible light photocatalytic activity. *Applied Surface Science* **430**, 234–242.

Gao, Y., Lin, J., Zhang, Q., Yu, H., Ding, F., Xu, B., Sun, Y. & Xu, Z. 2018 Facile synthesis of heterostructured YVO_4/g-C_3N_4/Ag photocatalysts with enhanced visible-light photocatalytic performance. *Applied Catalysis B: Environmental* **224**, 586–593.

Guan, Z. J., Wang, P., Li, Q. Y., Li, Y. W., Fu, X. L. & Yang, J. J. 2017 Remarkable enhancement in solar hydrogen generation from MoS_2-RGO/ZnO composite photocatalyst by constructing a robust electron transport pathway. *Chemical Engineering Journal* **327**, 397–405.

Guan, Z. C., Wang, H. P., Wang, X., Hu, J. & Du, R. G. 2018a Fabrication of heterostructured β-Bi_2O_3-TiO_2 nanotube array composite film for photoelectrochemical cathodic protection applications. *Corrosion Science* **136**, 60–69.

Guan, Z. C., Wang, X., Jin, P., Tang, Y. Y., Wang, H. P., Song, G. L. & Du, R. G. 2018b Enhanced photoelectrochemical performances of ZnS-Bi_2S_3/TiO_2/WO_3 composite film for photocathodic protection. *Corrosion Science* **143**, 31–38.

Hashemizadeh, I., Golovko, V. B., Choi, J., Tsang, D. C. W. & Yip, A. C. K. 2018 Photocatalytic reduction of CO_2 to hydrocarbons using bio-templated porous TiO_2 architectures under UV and visible light. *Chemical Engineering Journal* **347**, 64–73.

He, W., Sun, Y., Jiang, G., Huang, H., Zhang, X. & Dong, F. 2018 Activation of amorphous Bi_2WO_6 with synchronous Bi metal and Bi_2O_3 coupling: photocatalysis mechanism and reaction pathway. *Applied Catalysis B: Environmental* **232**, 340–347.

Hu, X. F., Deng, F., Huang, W. Y., Zeng, G. S., Luo, X. B. & Dionysiou, D. D. 2018 The band structure control of visible-light-driven rGO/ZnS-MoS_2 for excellent photocatalytic degradation performance and long-term stability. *Chemical Engineering Journal* **350**, 248–256.

Jiao, Y. Y., Huang, Q. Z., Wang, J. S., He, Z. H. & Li, Z. J. 2019 A novel MoS_2 quantum dots (QDs) decorated Z-scheme g-C_3N_4 nanosheet/N-doped carbon dots heterostructure photocatalyst for photocatalytic hydrogen evolution. *Applied Catalysis B: Environmental* **247**, 124–132.

Jing, J. P., Chen, Z. Y., Bu, Y. Y., Sun, M. M., Zheng, W. Q. & Li, W. B. 2019 Significantly enhanced photoelectrochemical cathodic protection performance of hydrogen treated Cr-doped $SrTiO_3$ by Cr^{6+} reduction and oxygen vacancy modification. *Electrochimica Acta* **304**, 386–395.

Katsumata, K.-i., Motoyoshi, R., Matsushita, N. & Okada, K. 2013 Preparation of graphitic carbon nitride (g-C_3N_4)/WO_3 composites and enhanced visible-light-driven photodegradation of acetaldehyde gas. *Journal of Hazardous Materials* **260**, 475–482.

Kiosidou, E. D., Karantonis, A., Sakalis, G. N. & Pantelis, D. I. 2018 Electrochemical impedance spectroscopy of scribed coated steel after salt spray testing. *Corrosion Science* **137**, 127–150.

Kong, L. Q., Yan, J. Q. & Liu, S. Z. 2018 Carbonyl linked carbon nitride loading few layered MoS_2 for boosting photocatalytic hydrogen generation. *ACS Sustainable Chemistry & Engineering* **7** (1), 1389–1398.

Li, Y., Zhou, M., Cheng, B. & Shao, Y. 2020 Recent advances in g-C_3N_4-based heterojunction photocatalysts. *Journal of Materials Science & Technology* **56**, 1–17.

Liang, H. O., Bai, J., Xu, T. & Li, C. P. 2020 Controllable growth of foxtail-like MoS_2 on one-dimensional carbon nanofibers with enhanced photocatalytic activity. *Vacuum* **172**, 109059.

Liu, Y., Zhang, Y. & Yuan, J. 2014 Influence of produced water with high salinity and corrosion inhibitors on the corrosion of water injection pipe in Tuha oil field. *Engineering Failure Analysis* **45**, 225–233.

Liu, Y. Z., Zhang, H. Y., Ke, J., Zhang, J. Q., Tian, W. J., Xu, X. Y., Duan, X. G., Sun, H. Q., Tade M, O. & Wang, S. B. 2018 0D (MoS_2)/2D (g-C_3N_4) heterojunctions in Z-scheme for enhanced photocatalytic and electrochemical hydrogen evolution. *Applied Catalysis B: Environmental* **228**, 64–74.

Liu, H. H., Tian, K. F., Ning, J. Q., Zhong, Y. J., Zhang, Z. Y. & Hu, Y. 2019a One-step solvothermal formation of Pt nanoparticles decorated Pt^{2+}-doped α-Fe_2O_3 nanoplates with enhanced photocatalytic O_2 evolution. *ACS Catalysis* **9** (2), 1211–1219.

Liu, Y. T., Zhang, Q. P., Xu, M., Yuan, H., Chen, Y., Zhang, J. X., Luo, K. Y., Zhang, J. Q. & You, B. 2019b Novel and efficient synthesis of Ag-ZnO nanoparticles for the sunlight-induced photocatalytic degradation. *Applied Surface Science* **476**, 632–640.

Ma, Z. Z., Song, K., Wang, L., Gao, F. M., Tang, B., Hou, H. L. & Yang, W. Y. 2019 WO_3/$BiVO_4$ Type-II heterojunction arrays decorated with oxygen-deficient ZnO passivation layer: a highly efficient and stable photoanode. *ACS Applied Materials & Interfaces* **11** (1), 889–897.

Marinoiu, A., Raceanu, M., Carcadea, E., Varlam, M. & Stefanescu, I. 2017 Low cost iodine intercalated graphene for fuel cells electrodes. *Applied Surface Science* **424**, 93–100.

Marinoiu, A., Andrulevicius, M., Tamuleviciene, A., Tamulevicius, T., Raceanu, M. & Varlam, M. 2020 Synthesis of well dispersed gold nanoparticles on reduced graphene oxide and application in PEM fuel cells. *Applied Surface Science* **504**, 144511.

Mo, Z., Xu, H., Chen, Z., She, X., Song, Y., Lian, J., Zhu, X., Yan, P., Lei, Y., Yuan, S. & Li, H. 2019 Construction of MnO_2/monolayer g-C_3N_4 with Mn vacancies for Z-scheme overall water splitting. *Applied Catalysis B: Environmental* **241**, 452–460.

Nguyen, V.-H., Mousavi, M., Ghasemi, J. B., Le, Q. V., Delbari, S. A., Shahedi Asl, M., Shokouhimehr, M., Mohammadi, M., Azizian-Kalandaragh, Y. & Sabahi Namini, A. 2021 In situ preparation of g-C_3N_4 nanosheet/FeOCl: achievement and promoted photocatalytic nitrogen fixation activity. *Journal of Colloid and Interface Science* **587**, 538–549.

Ong, W. J., Tan, L. L., Ng, Y. H., Yong, S. T. & Chai, S. P. 2016 Graphitic carbon nitride (g-C_3N_4)-based photocatalysts for artificial photosynthesis and environmental remediation: are we a step closer to achieving sustainability? *Chemical Reviews* **116** (12), 7159–7329.

Ou, W., Pan, J. Q., Liu, Y., Li, S., Li, H. L., Zhao, W. J., Wang, J. J., Song, C. S., Zheng, Y. Y. & Li, C. R. 2020 Two-dimensional ultrathin MoS_2-modified black Ti^{3+}–TiO_2 nanotubes for enhanced photocatalytic water splitting hydrogen production. *Journal of Energy Chemistry* **43**, 188–194.

Papailias, I., Todorova, N., Giannakopoulou, T., Ioannidis, N., Boukos, N., Athanasekou, C. P., Dimotikali, D. & Trapalis, C. 2018 Chemical vs thermal exfoliation of g-C_3N_4 for NOx removal under visible light irradiation. *Applied Catalysis B: Environmental* **239**, 16–26.

Qiu, P., Lai, Y. Y., Sun, X. L., Chen, C. F. & Ge, L. 2020 Potent n-type nanostructured cruciate flower-like Cu/Cu_2O films for photocathodic protection. *Materials Chemistry and Physics* **241**, 122311.

Ren, J. F., Qian, B., Li, J. Z., Song, Z. W., Hao, L. & Shi, J. S. 2016 Highly efficient polypyrrole sensitized TiO_2 nanotube films for photocathodic protection of q235 carbon steel. *Corrosion Science* **111**, 596–601.

Rodriguez, J., Mouanga, M., Roobroeck, A., Cossement, D., Mirisola, A. & Olivier, M. G. 2018 Study of the inhibition ability of benzotriazole on the Zn-Mg coated steel corrosion in chloride electrolyte. *Corrosion Science* **132**, 56–67.

Ryan, M. P., Williams, D. E., Chater, R. J., Hutton, B. M. & McPhail, D. S. 2002 Why stainless steel corrodes. *Nature* **415** (6873), 770–774.

Sadeghi Erami, R., Amirnasr, M., Meghdadi, S., Talebian, M., Farrokhpour, H. & Raeissi, K. 2019 Carboxamide derivatives as new corrosion inhibitors for mild steel protection in hydrochloric acid solution. *Corrosion Science* **151**, 190–197.

Shanavas, S., Mohana Roopan, S., Priyadharsan, A., Devipriya, D., Jayapandi, S., Acevedo, R. & Anbarasan, P. M. 2019 Computationally guided synthesis of (2D/3D/2D) rGO/Fe_2O_3/g-C_3N_4 nanostructure with improved charge separation and transportation efficiency for degradation of pharmaceutical molecules. *Applied Catalysis B: Environmental* **255**, 117758.

Shao, L. Q., Jiang, D. L., Xiao, P., Zhu, L. M., Meng, S. C. & Chen, M. 2016 Enhancement of g-C_3N_4 nanosheets photocatalysis by synergistic interaction of ZnS microsphere and RGO inducing multistep charge transfer. *Applied Catalysis B: Environmental* **198**, 200–210.

Shi, H. J. & Zhao, G. H. 2014 Water oxidation on spinel $NiCo_2O_4$ nanoneedles anode: microstructures, specific surface character, and the enhanced electrocatalytic performance. *The Journal of Physical Chemistry C* **118** (45), 25939–25946.

Sun, M. M., Chen, Z. Y. & Bu, Y. Y. 2015 Enhanced photoelectrochemical cathodic protection performance of the C_3N_4@In_2O_3 nanocomposite with quasi-shell–core structure under visible light. *Journal of Alloys and Compounds* **618**, 734–741.

Sun, J. W., Yang, S. R., Liang, Z. Q., Liu, X., Qiu, P. Y., Cui, H. Z. & Tian, J. 2020 Two-dimensional/one-dimensional molybdenum sulfide (MoS_2) nanoflake/graphitic carbon nitride (g-C_3N_4) hollow nanotube photocatalyst for enhanced photocatalytic hydrogen production activity. *Journal of Colloid and Interface Science* **567** (1), 300–307.

Vamvasakis, I., Papadas, I. T., Tzanoudakis, T., Drivas, C., Choulis, S. A., Kennou, S. & Armatas, G. S. 2018 Visible-light photocatalytic H_2 production activity of β-$Ni(OH)_2$-modified CdS mesoporous nanoheterojunction networks. *ACS Catalysis* **819**, 8726–8738.

Wang, X. C., Maeda, K., Thomas, A., Takanabe, K., Xin, G., Carlsson, J. M., Domen, K. & Antonietti, M. 2008 A metal-free polymeric photocatalyst for hydrogen production from water under visible light. *Nature Materials* **8** (3), 76.

Wang, J., Yang, Z., Yao, W. Q., Gao, X. X. & Tao, D. P. 2018a Defects modified in the exfoliation of g-C_3N_4 nanosheets via a self-assembly process for improved hydrogen evolution performance. *Applied Catalysis B: Environmental* **238**, 629–637.

Wang, R., Kong, X. Y., Zhang, W. T., Zhu, W. X., Huang, L. J., Wang, J., Zhang, X., Liu, X. N., Hu, N., Suo, Y. R. & Wang, J. L. 2018b Mechanism insight into rapid photocatalytic disinfection of *Salmonella* based on vanadate QDs-interspersed g-C_3N_4 heterostructures. *Applied Catalysis B: Environmental* **225**, 228–237.

Wang, Y. G., Xia, Q. N., Bai, X., Ge, Z. G., Yang, Q., Yin, C. C., Kang, S. F., Dong, M. D. & Li, X. 2018c Carbothermal activation synthesis of 3D porous g-C_3N_4/carbon nanosheets composite with superior performance for CO_2 photoreduction. *Applied Catalysis B: Environmental* **239**, 196–203.

Wang, Q., Wang, P., Xu, P., Li, Y., Duan, J., Zhang, G., Hu, L., Wang, X. & Zhang, W. 2020 Visible-light-driven photo-Fenton reactions using $Zn_{1-1.5x}Fe_xS$/g-C_3N_4 photocatalyst: degradation kinetics and mechanisms analysis. *Applied Catalysis B: Environmental* **266**, 118653.

Wei, N., Lin, Y., Li, Z. K., Sun, W. X., Zhang, G. S., Wang, M. L. & Cui, H. Z. 2019 One-dimensional Ag_2S/ZnS/ZnO nanorod array films for photocathodic protection for 304 stainless steel. *Journal of Materials Science & Technology* **42**, 156–162.

Xie, Z., Feng, Y., Wang, F., Chen, D., Zhang, Q., Zeng, Y., Lv, W. & Liu, G. 2018 Construction of carbon dots modified MoO_3/g-C_3N_4 Z-scheme photocatalyst with enhanced visible-light photocatalytic activity for the degradation of tetracycline. *Applied Catalysis B: Environmental* **229**, 96–104.

Xu, D., Cheng, B., Wang, W., Jiang, C. & Yu, J. 2018 Ag_2Cro_4/g-C_3N_4/graphene oxide ternary nanocomposite Z-scheme photocatalyst with enhanced CO_2 reduction activity. *Applied Catalysis B: Environmental* **231**, 368–380.

Xu, Y. S., He, X., Zhong, H., Singh, D. J., Zhang, L. J. & Wang, R. H. 2019 Solid salt confinement effect: an effective strategy to fabricate high crystalline polymer carbon nitride for enhanced photocatalytic hydrogen evolution. *Applied Catalysis B: Environmental* **246**, 349–355.

Yang, Y., Zeng, G., Huang, D., Zhang, C., He, D., Zhou, C., Wang, W., Xiong, W., Li, X., Li, B., Dong, W. & Zhou, Y. 2020 Molecular engineering of polymeric carbon nitride for highly efficient photocatalytic oxytetracycline degradation and H_2O_2 production. *Applied Catalysis B: Environmental* **272**, 118970.

You, J., Bao, W., Wang, L., Yan, A. & Guo, R. 2021 Preparation, visible light-driven photocatalytic activity, and mechanism of multiphase CdS/C_3N_4 inorganic-organic hybrid heterojunction. *Journal of Alloys and Compounds* **866**, 158921.

Zhang, J., Du, R. G., Lin, Z. Q., Zhu, Y. F., Ya, G., Qi, H. Q., Xu, L. & Lin, C. J. 2012 Highly efficient CdSe CdS cosensitized TiO_2 nanotube films for photocathodic protection of stainless steel. *Electrochimica Acta* **83**, 59–64.

Zhang, L. W., Reisner, E. & Baumberg, J. J. 2014 Al-doped ZnO inverse opal networks as efficient electron collectors in $BiVO_4$ photoanodes for solar water oxidation. *Energy Environment Science* **7** (4), 1402–1408.

Zhang, F. J., Li, X., Sun, X. Y., Kong, C., Xie, W. J., Li, Z. & Liu, J. 2019a Surface partially oxidized MoS_2 nanosheets as a higher efficient cocatalyst for photocatalytic hydrogen production. *Applied Surface Science* **487**, 734–742.

Zhang, X. C., Zhang, R. Y., Niu, S. Y., Zheng, J. M. & Guo, C. F. 2019b Enhanced photo-catalytic performance by effective electron-hole separation for MoS_2 inlaying in g-C_3N_4 hetero-junction. *Applied Surface Science* **475**, 355–362.

Zhang, Z. F., Dong, Y., Liu, G. Y., Li, J. W., Sun, H., Luo, H. & Liu, S. 2020 The ultrafine monolayer 1 T/2H-MoS_2: preparation, characterization and amazing photocatalytic characteristics. *Colloids and Surfaces A: Physicochemical and Engineering Aspects* **589**, 124431.

Zhou, X., Yu, H., Zhao, D., Wang, X. & Zheng, S. 2019 Combination of polyoxotantalate and metal sulfide: a new-type noble-metal-free binary photocatalyst $Na_8Ta_6O_{19}$/$Cd_{0.7}Zn_{0.3}S$ for highly efficient visible-light-driven H_2 evolution. *Applied Catalysis B: Environmental* **248**, 423–429.

Zhou, Q., Feng, J., Peng, X., Zhong, L. & Sun, R. 2020 Porous carbon coupled with an interlaced MoP–MoS_2 heterojunction hybrid for efficient hydrogen evolution reaction. *Journal of Energy Chemistry* **45**, 45–51.

First received 12 April 2021; accepted in revised form 8 June 2021. Available online 21 June 2021